Cotton-wool-like bioactive glasses for bone regeneration

Poologasundarampillai, Gowsihan; Wang, D.; Li, S.; Nakamura, J.; Bradley, R.; Lee, P. D.; Stevens, M. M.; McPhail, David S.; Kasuga, Toshihiro; Jones, J. R.

DOI:
10.1016/j.actbio.2014.05.020

Document Version
Publisher's PDF, also known as Version of record

Citation for published version (Harvard):
Poologasundarampillai, G, Wang, D, Li, S, Nakamura, J, Bradley, R, Lee, PD, Stevens, MM, McPhail, DS, Kasuga, T & Jones, JR 2014, 'Cotton-wool-like bioactive glasses for bone regeneration', *Acta Biomaterialia*, vol. 10, no. 8, pp. 3733-3746. https://doi.org/10.1016/j.actbio.2014.05.020

Acta Biomaterialia 10 (2014) 3733–3746

Contents lists available at ScienceDirect

Acta Biomaterialia

journal homepage: www.elsevier.com/locate/actabiomat

Cotton-wool-like bioactive glasses for bone regeneration

G. Poologasundarampillai [a,*], D. Wang [a], S. Li [a], J. Nakamura [b], R. Bradley [c], P.D. Lee [c], M.M. Stevens [a,d], D.S. McPhail [a], T. Kasuga [b], J.R. Jones [a]

[a] Department of Materials, Imperial College London, South Kensington, London SW7 2AZ, UK
[b] Department of Frontier Materials, Nagoya Institute of Technology, Nagoya 466-8555, Japan
[c] School of Materials, The University of Manchester, Oxford Rd., Manchester M13 9PL, UK
[d] Department of Bioengineering, Imperial College London, South Kensington, London SW7 2AZ, UK

ARTICLE INFO

Article history:
Received 12 November 2013
Received in revised form 13 May 2014
Accepted 16 May 2014
Available online 27 May 2014

Keywords:
Electrospinning
Sol–gel
Bone regeneration scaffold
3-D cotton-wool-like structure
Inorganic fibers

ABSTRACT

Inorganic sol–gel solutions were electrospun to produce the first bioactive three-dimensional (3-D) scaffolds for bone tissue regeneration with a structure like cotton-wool (or cotton candy). This flexible 3-D fibrous structure is ideal for packing into complex defects. It also has large inter-fiber spaces to promote vascularization, penetration of cells and transport of nutrients throughout the scaffold. The 3-D fibrous structure was obtained by electrospinning, where the applied electric field and the instabilities exert tremendous force on the spinning jet, which is required to be viscoelastic to prevent jet break up. Previously, polymer binding agents were used with inorganic solutions to produce electrospun composite two-dimensional fibermats, requiring calcination to remove the polymer. This study presents novel reaction and processing conditions for producing a viscoelastic inorganic sol–gel solution that results in fibers by the entanglement of the intermolecularly overlapped nanosilica species in the solution, eliminating the need for a binder. Three-dimensional cotton-wool-like structures were only produced when solutions containing calcium nitrate were used, suggesting that the charge of the Ca^{2+} ions had a significant effect. The resulting bioactive silica fibers had a narrow diameter range of 0.5–2 μm and were nanoporous. A hydroxycarbonate apatite layer was formed on the fibers within the first 12 h of soaking in simulated body fluid. MC3T3-E1 preosteoblast cells cultured on the fibers showed no adverse cytotoxic effect and they were observed to attach to and spread in the material.

1. Introduction

Bone tissue regeneration strategies aim to use synthetic temporary templates (scaffolds) to aid the natural healing of bone defects. Osteoblasts secrete bone extracellular matrix (ECM), which is composed of collagen fibrous structure, with mineralized calcium phosphate [1,2]. Therefore, in defects where load-bearing materials are not needed, an ideal biomaterial scaffold for bone regeneration might have a three-dimensional (3-D) fibrous structure that mimics the ECM [3–5] and can be easily pushed into position by a surgeon or dentist. The scaffolds are also required to be biocompatible, bioactive (bond with bone) and bioresorbable [6]. Bioactive glasses can form a rapid bond with bone through formation of a hydroxycarbonate apatite (HCA) surface layer on contact with body fluid, and through release of soluble silica and calcium ions that can stimulate osteoprogenitor cells to produce more bone [7].

Electrospinning is a versatile technique for producing continuous fibers with diameters ranging from nano- to micrometer, mimicking the fibers of ECM [8–10]. The high porosity and large surface area of the electrospun nanofibrous material provide numerous binding sites for protein adsorption and cell attachment [11]. Non-woven, aligned, crossed, layered and coaxial nanofibers with a high surface area can be produced by controlling the electrospinning parameters [9,12,13]. Nanofibers of numerous organic polymers have been produced [10] because of the ease of formation of a viscoelastic solution in a volatile solvent that can be easily electrospun.

Electrospun polymer fibermats have applications as vascular grafts and scaffolds for nerve, bladder matrix, lung and bone regeneration [14,15], using primarily bioresorbable and degradable natural and synthetic polymers [14,16–21]. However, bioactivity and enhancement of osteogenesis by the release of calcium ions and silica species are not provided by polymers alone.

The sol–gel process has been used to produce bioactive glass foam scaffolds for bone repair [22–24]. Recently, hydroxyapatite and silica-based bioactive and bioresorbable inorganic nanofibers

* Corresponding author. Tel.: +44 (0)75 0804 8322; fax: +44 (0)20 7594 6757.
E-mail address: gowsh.p@imperial.ac.uk (G. Poologasundarampillai).

http://dx.doi.org/10.1016/j.actbio.2014.05.020
1742-7061/

have been electrospun for biomedical applications from sol–gel solutions [25–31]. Kim et al. [26] and later Lu et al. [32] were the first to successfully electrospin silica-based bioactive glass nanofibers from a sol–gel solution, using polyvinylbutyral as the binder. Post-spinning, the fibermat was heat-treated at 700 °C to eliminate the organic phase. Further, Kim et al. [26] showed in vitro attachment and differentiation of bone marrow-derived stem cells on the bioactive nanofibrous scaffold and compared it with bioactive glass films of the same composition. Cells cultured on the nanofibers showed enhanced ALP expression compared with those grown on discs of the same glass.

So far, all the electrospun bioactive sol–gel-derived nanofibers reported have been produced using a polymer binding agent; the calcination of the fibers at high temperature leads to embrittlement and partial crystallization. However, Ma et al. [33] produced bioactive core–shell structured fibermats through a two-step method without using a polymer binding agent. First, they electrospun silica fibers [34], which were then coated with a bioactive glass shell by immersion in a modified Stöber sol.

Structurally, all the inorganic fibermats reported in the literature were two-dimensional (2-D) with small inter-fiber spacing. Three-dimensional scaffolds are necessary to act as templates and regenerate bone in large defects, and it is estimated that the interconnected spaces >100 μm are required for vascularized bone tissue growth [35]. The fiber–fiber separation distance (pore size) in a fibermat is related to the fiber diameter, where larger fiber diameter leads to larger fiber–fiber separation distances. For a fibermat, fiber diameters >∼20 μm are recommended to create a stable mat with a pore size >100 μm [36]. These fibers are approximately the diameter of an osteoblast, and therefore the cells interact with the fibermat as they would on solid material. Therefore, such mats do not mimic the ECM.

The aim here was to develop an electrospun bioactive glass scaffold with smaller fiber diameters in the range 0.3–1 μm [4,11], with a 3-D macroporous architecture. In electrospinning, the term "3-D" is often associated with 2-D fibermats that are thicker (∼0.5–2 mm) than conventional fibermats (<0.5 mm) [37–39]. This does not increase the inter-fiber distance of the fibermat. Here, it is important to define the cotton-wool-like structured materials as a separate and superior class of 3-D scaffolds. Recently, melt-derived Bioglass fibres were produced by laser spinning [40], and work by Mo-Sci Corp in the USA recently showed that melt-derived "cotton-candy" borate fibers produced good clinical results, healing chronic diabetic foot ulcers [41]. The inventors used melt blowing to produce fibers with a range of fiber diameters for wound regeneration. For bone regeneration, Stark et al.'s group [42] was one of the first to use the term "cotton-wool-like" for electrospun fibers of poly(lactide-*co*-glycolide)/amorphous tricalcium phosphate nanocomposite material. Later, Obata et al. [43] also electrospun poly(L-lactic acid) and siloxane-doped vaterite (SiV) composite cotton-wool-like fibers. Both had a structure similar to cotton-wool, but they both employed a post-electrospinning process to produce the cotton-wool-like structure: a manual fiber unravelling method in the case of Schneider et al. [42] and a fan method in the case of Obata et al. [43].

In the present work, the sol–gel processing was used in combination with electrospinning to produce the first bioactive sol–gel silica 3-D cotton-wool-like structured scaffolds for bone regeneration.

2. Materials and methods

The silica precursor tetraethylorthosilicate (TEOS) was purchased from Sigma–Aldrich, and all other chemicals for the synthesis of the sol–gel electrospun fibers were purchased from Wako Pure Chemical Industries, Ltd., Osaka, Japan.

2.1. Fiber production

2.1.1. Sol–gel precursor solution preparation

The hydrolysis and condensation of TEOS to Si–O–Si linear chains under acid catalysis with an R ratio (H_2O:TEOS) of 2 has been reported by several groups for drawing silicate fibers [44–46]. Following this method, 100 mol.% SiO_2 (100S) precursor solutions for electrospinning were first prepared by mixing, in the order TEOS, ethanol, water and 1 N HCl to a final molar ratio of TEOS:ethanol:water:HCl of 1:2:2:0.01. The mixture was stirred for 24 h at room temperature. Calcium-containing fibers with a nominal composition of 70 mol.% SiO_2 and 30 mol.% CaO (70S30C) were prepared by the addition of calcium nitrate tetrahydrate ($Ca(NO_3)_2{\cdot}4H_2O$) after 1 h of mixing TEOS, ethanol and 1 N HCl. A final ratio of TEOS:ethanol:water:HCl:$Ca(NO_3)_2$ of 1:2:2.23:0.01:0.3 was obtained. The 70S30C precursor solution was also left to react (age) for 24 h then heated at 70 °C in an oven, while continuously mixing to increase the viscosity of the sol. The solution viscosities of 100S and 70S30C were measured before and after the evaporation of ethanol, using a TOKI, RE-80H cone rotor viscometer. Ten viscosity measurements were performed in 5 min on 1 ml of solution, and the mode was selected as the actual viscosity. Table 1 lists the quantities of the reagents used and the amount of solvent evaporated. After the evaporation of ethanol, the sol–gel precursor solutions were loaded into a metallic needle (22 gauge), attached to a glass syringe and spun on the Nanofiber Electrospinning Unit (NEU, Kato Tech Co, Japan). The high-tension field was applied to the metal needle. The fibers were collected on Teflon-coated aluminum foil placed on a rotating drum that was positioned at a distance of 100 mm from the capillary. The electrospinning conditions used for spinning both solutions are listed in Table 1. The electrospun fibers were then transferred to an oven and heat-treated at 60 °C for 72 h.

Images and videos of electrospinning were obtained using an Olympus Pen lite E-PL1 camera equipped with 60× zoom and shutter speeds of 1/2000 s. Brightness and contrast of the photos were enhanced in ImageJ.

2.2. Characterization

2.2.1. Morphology and physical structure

Low magnification images of the fibers were produced by scanning electron microscopy (SEM; JSM-6301). Samples were coated with amorphous osmium using an Os coater and observed under 5 kV accelerating voltage and 15 mm working distance. High-magnification images were obtained by SEM on a LEO-1525 microscope equipped with a GEMINI field emission column. Samples were sputter coated with chromium to a maximum coating thickness of 13 nm before imaging. An operating voltage of 5 kV and working distances of 5–8 mm were used. Transmission electron microscopy (TEM) images were collected on a JEOL 2010 equipped with a LaB_6 filament. An operating voltage of 200 kV was used on samples thinner than 100 nm, prepared using a focused ion beam (FIB; Helios NanoLab 600) miller. FIB was used to section thin slices from 70S30C samples embedded in epoxy resin.

2.2.2. Chemical and atomic structure

A time-of-flight secondary ion mass spectroscopy (TOF-SIMS) instrument (ION–TOF GmbH, Germany) was applied to determine the distribution of silicon and calcium along the electrospun 70S30C bioactive glass fibers. A 25 keV Bi_3^+ primary ion source with a current of 0.1 pA was used to construct the secondary ion maps (512 × 512 pixels) on a 130 × 130 μm^2 area at an accumulated ion dose intensity of 1.21×10^{13} ions cm^{-2}. A low-energy 20 eV electron flood gun was used for charge compensation. Attenuated total reflectance–Fourier transform infrared spectroscopy (ATR-FTIR), X-ray diffraction (XRD), ^{29}Si magic angle spinning nuclear

Table 1
Summary of the electrospinning solution properties and the conditions used in the production of long fibers.

Sample	TEOS (ml)	Ethanol (ml)	H_2O (ml)	1 N HCl (ml)	$Ca(NO_3)_2{\cdot}4H_2O$ (g)	Solvent evaporated (wt.%)	Viscosity (Pa·s)	Flow rate ($\mu l\ s^{-1}$)	Voltage (kV)	N–C (mm)[a]
100S	17.1	8.8	2.0	0.7	–	63	0.29–0.56	0.53	15	10
70S30C	17.1	8.8	0.0	0.7	7.67	40–43	0.56–0.95	0.68	15	10

[a] N–C = needle to collector distance.

magnetic resonance (MAS-NMR) and differential thermal analysis–thermogravimetry analysis (DTA-TGA) were performed to analyze the atomic, chemical structure and thermal properties of the electrospun sol–gel-derived fiber material. Fiber samples were ground to a fine powder, and XRD measurements were performed on a PhilipsX'PertPro fitted with an X'Celerator detector. Spectra were collected between 10 and 70° in 2θ with a step size of 0.016711. ^{29}Si MAS-NMR spectra of the sol–gel-derived samples were recorded on Varian UnityPlus 400 (Varian, USA) spectrometer operating at 79.46 MHz, using a 7.5 mm Varian probe spinning at 5 kHz. Around 2200 scans were collected at 4.5 μs pulse with 30 s recycle delay. Spectra were deconvoluted using Dmfit [47]. DTA-TGA was measured on the fiber samples using a Rigaku ThermoPlus (TG 8120) at a heating rate of 10 °C min^{-1}.

2.2.3. Porosity and pore structure

N_2 sorption was performed on a Quantochrome Autosorb1® after outgassing at ambient temperature for 12 h to investigate the mesoporosity and the surface area of the electrospun materials. Mercury intrusion porosimetry (MIP) was performed on a Quantochrome Poremaster instrument to obtain the pore size distribution of the fibers. Microcomputed tomography (μCT) was performed on the 70S30C fibers to image the 3-D arrangement of fibers. The 70S30C fibers were first cold mounted in epoxy to avoid movement during the scan on a Xradia VersaXRM-500. Scans were produced with a voxel size of 0.8442 μm and imaged on Avizo visualization software.

2.3. Handling properties and compression testing

To demonstrate the handling properties of the 70S30C cotton-wool-like samples, they were packed in printed plastic models of tooth extraction sockets. Compression tests were carried out on a Zwick mechanical tester loaded with a 500 N load cell. Samples were loaded to 10 N (160 kPa) at 0.5 mm min^{-1} and unloaded to obtain the load vs. deformation hysteresis curves under a confined compression setup. Samples with three different initial densities were produced by packing increasing amounts of samples to a constant volume.

2.4. Apatite formation tests in simulated body fluid

Simulated body fluid (SBF) was prepared according to the procedure given by Kokubo et al. [48,49] using chemicals purchased from Chameleon Reagents. Rectangular fibermats of 100S and 7.5 mg of 70S30C cotton-wool-like fibrous material were immersed in 15 ml of SBF for 1–168 h, with a sample to SBF ratio of 0.5 mg ml^{-1}. The immersed samples were placed in an incubator, which was kept at a constant temperature of 36.5 °C to mimic physiological temperature. After the pre-determined immersion time period, the pH of the solution was measured, and then the samples were removed and washed with deionized water and dried in air. The soluble silica and phosphate species and Ca^{2+} ion concentrations in the SBF were measured by inductively coupled plasma–atomic emission spectroscopy (ICP-AES) (ICPS-500, Shimadzu, Japan). FTIR, XRD and SEM were also performed to determine the formation of apatite on the samples.

2.5. In vitro cell culture

All cell culture reagents were obtained from Invitrogen and Sigma–Aldrich UK unless specified otherwise. MC3T3-E1 pre-osteoblast cell line (ATCC, UK) was culture expanded in monolayer cultures in basal α-MEM supplemented with 10% (v/v) fetal calf serum, 100 unit ml^{-1} penicillin and 100 μg ml^{-1} streptomycin. Cultures were maintained in a humidified atmosphere at 37 °C, 5% CO_2 and 21% O_2. Upon confluence, cells were passaged using 500 μg ml^{-1} trypsin–EDTA (ethylene diamine tetra-acetic acid).

For cell culture on 70S30C cotton-wool-like fibrous scaffolds, electrospun 70S30C cotton-wool-like fibrous scaffolds were divided into 1.5 mg aliquots and sterilized with 70% ethanol for 1 min. Following washing with PBS, each sample was preconditioned for 3 days in serum-free α-MEM (1 ml) in humidified atmosphere at 37 °C, 5% CO_2 and 21% O_2. Each preconditioned sample was transferred to a sterile 15 ml centrifuge tube and centrifuged at 400*g* in order to create a compact fiber network.

Monolayer cultured MC3T3-E1 cells were harvested and suspended in basal α-MEM at a concentration of 5×10^5 cells ml^{-1}. One milliliter of cell suspension was added to each 15 ml centrifuge tube containing the compact 70S30C cotton-wool-like fibrous scaffold and incubated in humidified atmosphere at 37 °C, 5% CO_2 and 21% O_2 for 2 h, with gentle agitation every 30 min to allow diffused cell adhesion. The culture media was then replaced with fresh basal α-MEM, and the cell-seeded samples were cultured for a further 3 days.

Day-3 cell-seeded 70S30C cotton-wool-like fibrous scaffolds were fixed with 2% glutaraldehyde and 1% osmium tetroxide and dehydrated using an ascending series of ethanol. Following freeze drying and sputter coating with gold, SEM was performed to image the attachment and morphology of cells on fibers, using the Auriga FIB-SEM at an acceleration voltage of 5 kV in the secondary electron mode.

To determine the potential cytotoxicity effect of 70S30C cotton-wool-like fibrous material on MC3T3-E1 cells, dissolution products released from the sample (with and without preconditioning, 1.5 mg ml^{-1} in α-MEM) over a 3-day period were prepared. The dissolution products were filter sterilized and supplemented with 10% (v/v) prior to use in cell viability assays. Cell viability was assessed using a calorimetric cell metabolic activity assay based on the conversion of 3-(4,5-dimethylthiazol-2-yl)-2,5-diphenyltetrazolium bromide (MTT) into formazan [50]. MC3T3-E1 cells were seeded on 96-well plates at 1×10^4 cells per well and left to grow in basal α-MEM for 24 h until a sub-confluent monolayer was formed. The culture media was removed, and MC3T3-E1 cells were then incubated with the dissolution products (100 μl per well) of 70S30C cotton-wool-like fibrous material for a further 1, 3 and 6 days. At each time point, the culture media was removed, and then MTT diluted in serum-free α-MEM at a concentration of 1 mg ml^{-1} was added (100 μl per well). Following an incubation period of 3 h, the MTT solution was removed, and each well was filled with 100 μl DMSO and shaken for 5 min to dissolve the formazan derivatives. The opti-

cal density was measured spectrophotometrically at 570 nm, using a microplate reader (SpectraMax M5).

3. Results and discussion

3.1. Electrospinning of sol–gel-derived silica fibers

Electrospinning requires a viscoelastic solution that has the ability to stretch under high elongational forces, while resisting break-up. Materials with long chains dissolved in a suitable volatile solvent are ideal for electrospinning. Inorganic materials that behave like polymers are difficult to produce; sol–gel processing offers one of the best methods of realizing this goal.

When the 100S sol was electrospun, a conventional 2-D fibermat was produced, but when the 70S30C composition was electrospun, a 3-D fibrous structure formed.

Fig. 1a shows the SEM image of 70S30C electrospun material immediately after aging for 24 h. The low viscosity (0.03 and 0.04 Pa·s for 100S and 70S30C, respectively) of the precursor solution led to spraying, which resulted in the production of whiskers. A higher viscosity solution was required to produce fibers; this was achieved by heating the precursor solution at 70 °C, while stirring continuously with a magnetic stirrer. Fig. 1a–d shows the morphology of the materials produced after heating to increase the viscosity, while Fig. 1e shows the viscosity of the solution as a function of solvent evaporated. Heating the precursor solution increased the viscosity of the spinning solution by (1) evaporation of ethanol and (2) catalyzing the condensation reaction of hydrolyzed TEOS. On heating, the viscosity initially increased slowly as a result of evaporation of ethanol and water. After the evaporation of 42 wt.% solvent, the viscosity was observed to increase rapidly, owing to the condensation and crosslinking of colloidal silica species.

Electrospinning the heat-evaporated sol–gel solution after ~32 wt.% solvent evaporation at a viscosity of 0.25 Pa·s produced short fibers (Fig. 1b). After evaporation of up to 40–43 wt.% solvent, stable long-continuous fibers (Fig. 1c) formed. This corresponded to a viscosity in the range 0.56–0.95 Pa·s. Electrospinning a more highly viscous solution (>2.77 Pa·s) produced large beads, rather than fibers, as a result of extensive condensation of silica species leading to particles that agglomerated on deposition. Therefore, for the production of continuous fibers of 70S30C, a precursor solution with a viscosity of 0.56–0.95 Pa·s and between 40 and 43 wt.% solvent evaporation was required. This is indicated in Fig. 1e as the narrow region C on the "solvent evaporated vs viscosity" graph. The 100S (100 mol.% SiO_2) composition was electrospun for comparison.

More evaporation of solvent was required for 100S, with up to 63 wt.% solvent evaporation needed to achieve a solution viscosity of 0.56 Pa·s. Continuous fibers were produced from an aged and evaporated sol with viscosity in the range 0.29–0.56 Pa·s (Fig. 2a), therefore sol of the 100S composition can be electrospun into fibers at a lower viscosity than the 70S30C composition. The 100S sol with a viscosity outside the range 0.29–0.56 Pa·s did not result in continuous fibers.

Fig. 2 shows the SEM images of the sol–gel-derived fibers 100S (a, c, e) and 70S30C (b, d, f). Continuous or long fibers of both compositions were successfully produced. The 100S and 70S30C samples had a homogeneous fiber morphology, as shown in the SEM images in Fig. 2a and b. Mean fiber diameters were measured (n = 20) from SEM images and are summarized in Table 2. The fiber diameter ranged between 0.5 and 2.0 μm for both samples. This shows that the sol–gel precursor solutions were very stable for the duration of spinning. High-magnification images show that the 70S30C fiber (Fig. 2d) had a rough and porous structure, while the 100S (Fig. 2c) had a smooth surface. Higher-magnification SEM images were obtained of the fiber fracture surface, which showed that both 100S (Fig. 2e) and 70S30C (Fig. 2f) fibers had interconnected mesoporous structures of fused nanoparticles typical of the acid-catalyzed sol–gel glasses [51]. The size of the particles was measured from the SEM images to be in the range 10–25 nm for the 70S30C, while that of 100S was found to be <10 nm.

The cross-sectional SEM image of a 70S30C fiber (Fig. 3a) shows that the 70S30C material was highly porous with numerous pores <200 nm. FIB milling was also employed to produce electron-transparent thin sections of the cross sections of the 70S30C fibers for imaging with TEM (Fig. 3b). The TEM imaging (Fig. 3c) shows that the fibers were nanoporous with pores <30 nm. Energy dispersive maps of Si (Fig. 3d) and Ca (Fig. 3e) were overlaid to produce a color map representing the distribution of Si and Ca across the cross section of the fiber (Fig. 3f) to show that Si and Ca were distributed throughout the cross section of the fiber and that there was no noticeable separation of Si and Ca along the cross section of the fiber.

The 3-D structure created by spinning the 70S30C sol is unusual, so it was important to understand how it formed. The electrospinning process has been described in detail, and extensive mathematical models have been developed by Reneker et al. [52,53]. Briefly, during electrospinning, the application of a high voltage on the spinning solution forces the liquid at the tip of the capillary to deform into a conical shape, often called a Taylor cone. Once the electric field between the cone and the collector exceeds a threshold value; a jet of solution is ejected in the direction of the electric field. This then undergoes bending and whipping instabilities, during which the fiber stretches, thins and solidifies as it travels to the collector. At the grounded collector, the fiber discharges. Fig. 4a and b shows optical images taken during the electrospinning of 100S and 70S30C fibers, respectively. The electrospinning of 100S followed a typical mechanism (Fig. 4a). A Taylor cone (indicated by ∗) was followed by a stable jet (indicated by +), leading to bending and whipping instabilities, which were observed through to the collector. Fig. 4a shows that a continuous fiber was formed, and it was maintained until the end of spinning, resulting in a 2-D non-woven fibermat.

The electrospinning of 70S30C precursor solution resulted in a 3-D cotton-wool-like fibrous structure (Fig. 4c and Supporting information 1). Fig. 4b shows the electrospinning of the 3-D cotton-wool-like structure. During electrospinning of 70S30C, a Taylor cone formed (∗ in Fig. 4b) and a jet (+ in Fig. 4b) was also obtained. Later; the jet split into a few branches before the bending instabilities took effect.

Yarin et al. [54] reported observation of multiple branches of jets off a primary polymer jet at the location near a large diameter capillary tip. The excess charge carried by the primary jet gave rise to radial forces that led to branches of jets being ejected off the primary jet. In the case of 70S30C, the presence of Ca^{2+} ions increased the charge density on the surface of the jet [55], and hence large radial forces were generated that overcame the cohesive forces within the jet, leading to branching. However, rather than branches coming off a primary jet; it split into several jets, described as splaying by Reneker et al. [8]. The splaying of the jet is due to the lower viscoelasticity of the inorganic precursor solution (a high viscoelastic polymer jet would branch). The splayed 70S30C jets repel each other and separate, but owing to the influence of electric potential, they still moved towards the collector. The jets then underwent normal bending instability with the fiber axis in the direction perpendicular to the electric potential. The fiber axis then changed again in the direction parallel to the electric potential. This reorientation after the bending instability is due to the conductivity of the 70S30C fibers. Srinivasan [56] and Reneker et al. [53] reported the reorientation and entanglement of conductive

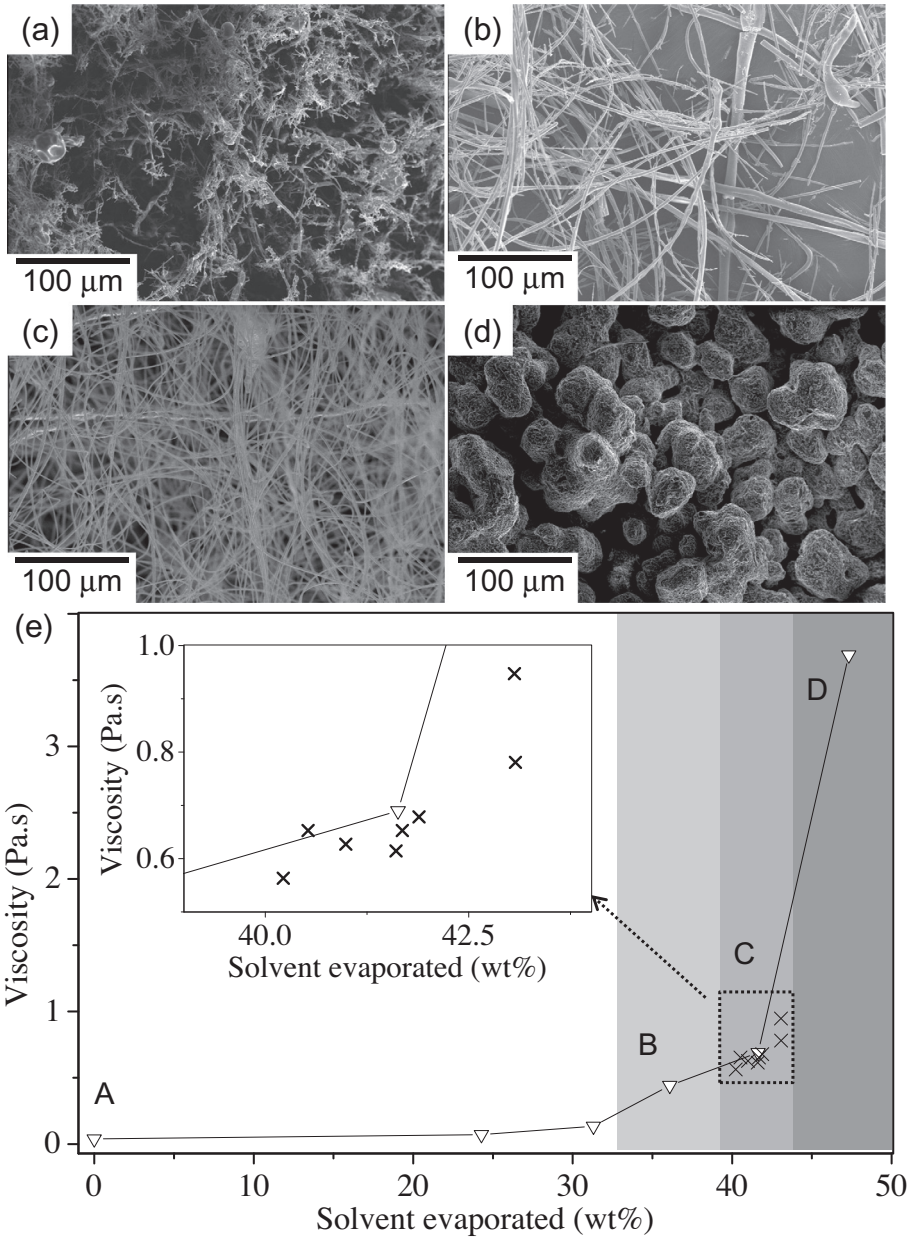

Fig. 1. SEM-SE images of the morphology of 70S30C electrospun (a) whiskers, (b) short fibers, (c) long fibers and (d) electro-sprayed beads, with increasing (e) viscosity as a function of solvent evaporated. The percentage of solvent evaporated at 70 °C and viscosity of samples a, b, c and d were (A) 0%, (B) 32%, (C) 40% and (D) 47% and 0.04, 0.25, 0.95 and >2.77 Pa·s, respectively.

polymer polyaniline during electrospinning. They found that the dry polyaniline nanofibers formed networks and entangled in the direction of the applied electric field, rather than forming a flat non-woven mat. They concluded that the conductivity of polyaniline allowed for the electronic charge to redistribute and accumulate at favorably oriented ends or bends in the fibers and stretched the fibers in the direction of the applied field.

In the 70S30C fibers, the charge carriers were Ca^{2+} and NO_3^-, and they could diffuse through the water in the silica gel fibers, making the 70S30C fibers conductive. The 70S30C fibers also formed network and entanglement (Supporting information 1). The 70S30C fibers were only temporarily conductive, and as soon as the gel fibers dried and the water evaporated, the fibers became insulating, but by this time the fibers had already discharged on the collector as a 3-D network of entangled fibers resembling a cotton-wool-like structure.

TOF SIMS was performed to assess the distribution of Si and Ca along the fiber. A heterogeneous distribution of Si and Ca suggests that the SiO^{4-} and Ca^{2+} migrated under the influence of the external electric field. Fig. 5a shows a SEM image of a single fiber embedded in an epoxy matrix, which was then scanned using TOF SIMS. Fig. 5b and c shows the distribution of Si and Ca along the fiber obtained using TOF SIMS, where red is high intensity, and blue/black indicates low intensity. Insets in Fig. 5b and c show that section A of the fiber was depleted of Si and rich in Ca, while section B was rich in Si and Ca was low. This may suggest that, although at the solution stage both Si and Ca were homogeneously distributed, once electrospun, Si and Ca partially separated out, owing to the movement of charged ions through the fluid in the gel phase as a result of the applied electric field. The position and concentration of the charges along the fiber will dictate the overall forces experienced by that fiber during electrospinning. It

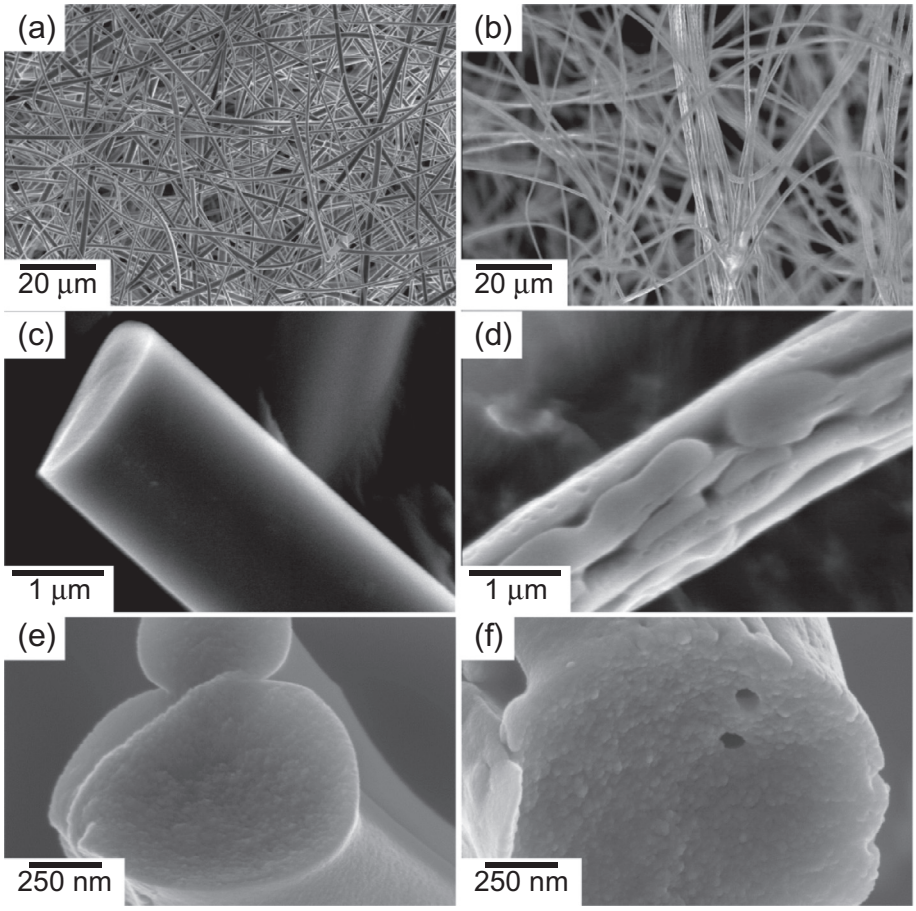

Fig. 2. Low and high magnification SEM-SE images of the electrospun sol–gel-derived fibers (a,c,e) 100S and (b,d,f) 70S30C. The high magnification images show the smooth surface profile of 100S fibers and the nanoporous structure of the 70S30C.

Table 2
Inorganic fiber macro architecture, fiber diameter and N_2 sorption results of the electrospun sol–gel-derived fibers.

Sample	Macro architecture	Ave. fiber diameter (μm)	N_2 adsorbed ($cm^3\ g^{-1}$)	Surface area ($m^2\ g^{-1}$)
100S	2-D	1.0 ± 0.4	20.6	40.0
70S30C	3-D	1.5 ± 0.4	26.7	34.6

is observed in Fig. 4b that, after the bending instability, the fibers reoriented again in the direction of the electric field. Here, it is supposed that the regions along the fiber that have higher concentration of Ca^{2+} would travel faster towards the collector. This leads to stretching of the wet fiber. Thus, regions that travelled faster and stretched would form bends that are likely to be rich in Ca^{2+}. This could also happen in the ends of fibers, where Ca^{2+} would favorably concentrate. Fig. 5d shows the overlap of Si and Ca ion distributions in the fiber images in Fig. 5a. It shows that the bent section at the middle of the fiber was rich in Ca, while the ends were depleted of Ca. Fig. 5e also shows TEM energy dispersive X-ray (EDX) analysis of two, bent and straight, sections of the 70S30C fibers normalized with Si atomic count. The inset in Fig. 5e shows the Ca count was higher in the bent section compared with the straight section by more than 30%. This also supports the finding of TOF SIMS. Hence, the addition of Ca^{2+} in the sol–gel solution had produced an effect similar to that of electrospinning polyaniline, as observed by Srinivasan [56] and Reneker et al. [53], where the charge carriers in a fiber that are present in an external electric field would concentrate at regions of favorable bends and ends through a conductive medium. Therefore, the formation of the 3-D cotton-wool-like structure of the 70S30C composition was due to several factors: the rheological properties and surface tension of the solution, which leads to branching and splaying, and the concentration of ionic species for conduction. In contrast, the 100S fibers could only form a 2-D non-woven mat, as they did not have any ions to act as charge carriers.

This is the first time that a 3-D-cotton-wool-like fibrous structure from a sol–gel precursor solution employing a simple electrospinning setup has been reported. Further, for bone regeneration, it is the first time that a calcium-containing inorganic fibrous material has been produced without using a polymeric binding agent such as poly(vinyl alcohol), as used by Kim et al. [26]. The fiber embrittlement resulting from the calcination of polymer from the composite fibers was avoided in this system. Owing to the 3-D nature of the material, it was found that more than 300 cm^3 of the material could be produced within 1 h of electrospinning.

Nitrogen sorption was performed to test the porosity of the fibers (Table 2). The 100S and 70S30C fibers had surface areas of 40.0 and 34.6 $m^2\ g^{-1}$, respectively. The amount of N_2 adsorbed and the surface area of the electrospun fibrous materials was lower compared with sol–gel glass foams and particles [24,51]. This indicates that the electrospun fibers were less porous and more highly condensed than the conventional sol–gel-derived glasses. However, they had a higher surface area compared with electrospun polymer materials such as PLLA with a similar fiber diameter, which have a surface area of <5 $m^2\ g^{-1}$. The higher surface area of the sol–gel-derived bioactive glass fibers was potentially due to the mesoporosity of the sol–gel-derived materials. The high

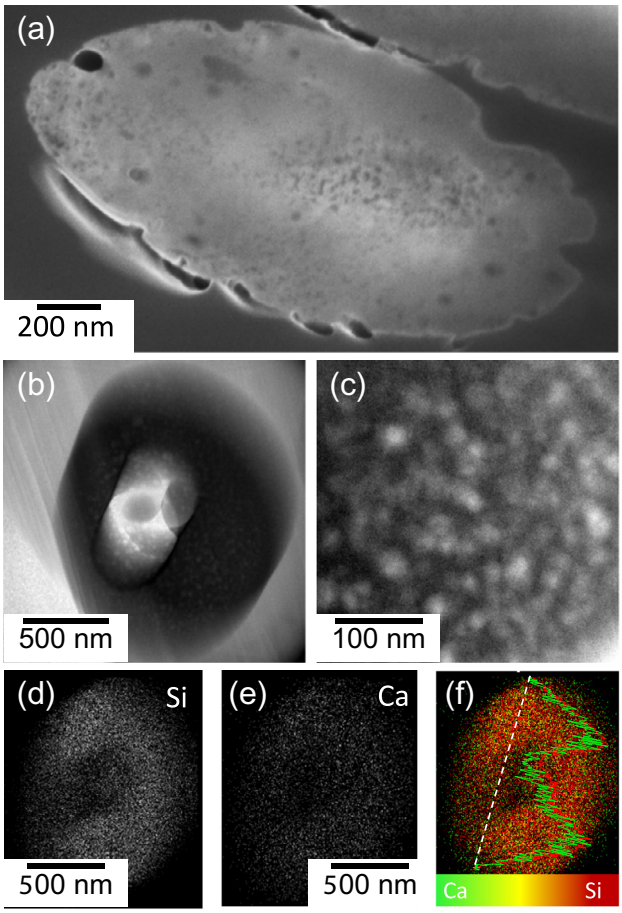

Fig. 3. Cross-sectional images and elemental maps of the 70S30C fibers. High magnification (a) SEM-SE and (b,c) TEM images of cross section of 70S30C fiber showing the internal porous architecture. EDX maps showing (d) Si, (e) Ca and (f) overlay of Si (red) and Ca (green) from the cross section in (b).

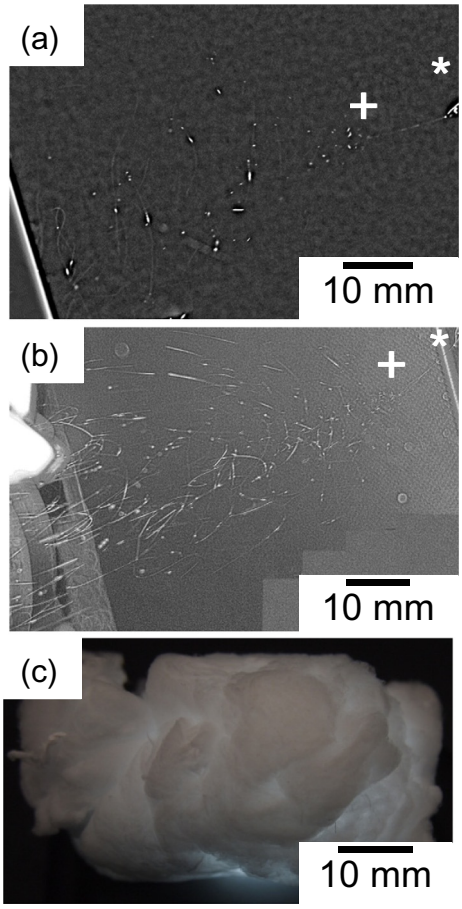

Fig. 4. Optical images showing the electrospinning of (a) 100S and (b) 70S30C and (c) photo of electrospun 70S30C cotton-wool-like material. Images (a) and (b) have been enhanced with ImageJ to clearly show the fibers. The bright white spots and streaks towards the collector are glints, which occur on segments of wet fibers oriented in such a way that the light from the camera flash is reflected into the camera. The + and ∗ on images are used to indicate the positions of the Taylor cone and start of bending instability.

magnification SEM images of 100S and 70S30C in Fig. 2c–f show that the 70S30C fibers were macroporous, with irregular pores in the range of several hundred nanometers to a few microns. The 100S had a smooth appearance, therefore the 100S was mesoporous, while the 70S30C fibers were macroporous and mesoporous.

3.2. Characterization of silica structure

Fig. 6 shows the ^{29}Si MAS NMR spectra, XRD pattern, FTIR spectra and DTA-TGA curves of the sol–gel-derived fibers dried at 60 °C. The deconvoluted proportions of ^{29}Si MAS NMR spectra enabled identification of Q^n species (where n represents the number of bridging oxygen that connects to the Si: 0, 1, 2, 3 or 4) and calculation of the degree of condensation (D_c calculated using Eq. (1)) and values are given in Table 3.

$$D_c = \frac{1 \times Q^1 + 2 \times Q^2 + 3 \times Q^3 + 4 \times Q^4}{4} \times 100\% \quad (1)$$

Both compositions have three chemical shifts typically at −92, −101 and −111 ppm, which were assigned to Q^2, Q^3 and Q^4 species, respectively. The 100S and 70S30C fibers have a large proportion of Q^4 (>60%) and a very small amount of Q^2 species with a D_c of ∼90%. This result is similar to the data published by Lin et al. [51] on conventional sol–gel-derived glasses with the compositions 100S and 70S30C. They calculated a network connectivity of 3.5 and 3.65 for the 100S and 70S30C samples, which translates to a D_c of 87.5 and 91.3%, respectively. However, heating the 70S30C glasses to 600 °C saw a decrease in D_c to 65.5% as the calcium entered the silica network as a network modifier. The high D_c of the fibers (>90%) in this work indicates that the calcium in the 70S30C fibers was not fully incorporated in the silica network.

Viscoelastic solutions composed of material with high molar mass and polymeric structures are required to cause entanglement and chain overlap for the production of continuous fibers [57]. This means that electrospinning of the sol–gel solution in the present study should not have resulted in fibers, as the solutions were composed of colloidal particles [51]. However, McKee et al. [58] proposed a model that has relevance to the present study by successfully electrospinning phospholipid non-woven fibermats from a solution containing lecithin. They suggested that the presence of sufficient intermolecular interactions between small molecules of ordered cylindrical micelles leads to chain entanglement and overlap, which enables fiber production. Therefore, in the present study, the colloidal silica nanoparticles in the sol–gel precursor solution have sufficient interaction for entanglement by hydrogen bonding, which prevents the electrospinning jet from breaking up. This was true for the electrospinning of 100S, where the fiber jet was observed not to break up even during bending and whipping instability. However, in the case of 70S30C, the addition of $Ca(NO_3)_2$, caused the breakup of the wet jet by increasing the conductivity, which leads to increased stretching of the wet gel.

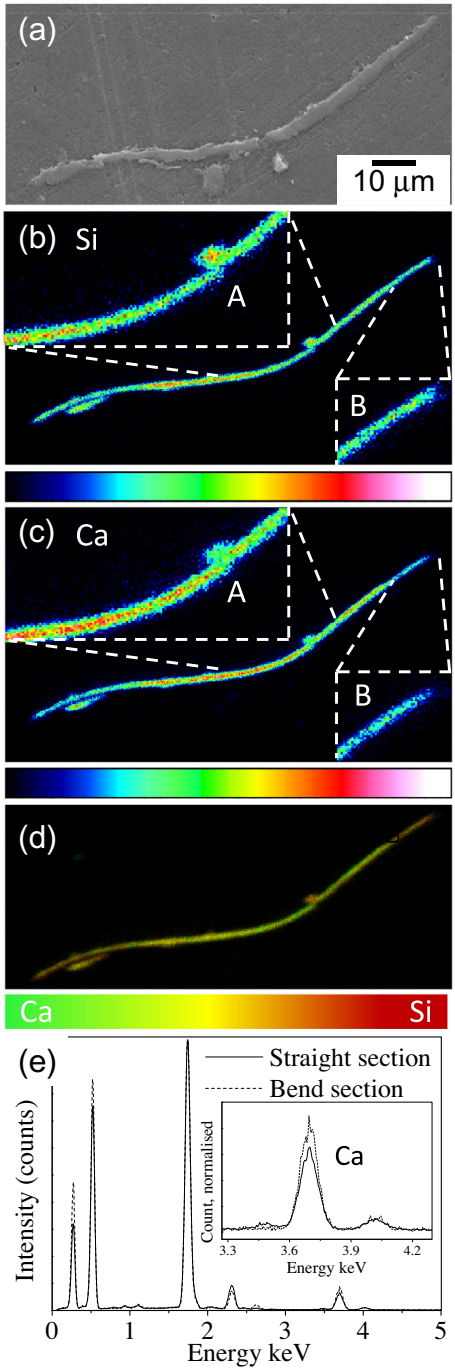

Fig. 5. (a) SEM image of a 70S30C fiber embedded in epoxy and ToF-SIMS secondary ion maps of (b) Si and (c) Ca profiles from the same fiber. Insets in (b) and (c) show regions along the fiber with local variation in Si and Ca concentrations. (d) Overlay of (b) and (c), where green means a high Ca concentration in the fiber, and orange means a high Si concentration. (e) EDX spectroscopy from the cross sections of the 70S30C fibers at straight and bend sections.

Further, McKee et al. [58] also showed that the solute concentration of the electrospinning solution must exceed the solute entanglement concentration for fibers to be produced. The evaporation of ethanol from the sol–gel precursor solution by aging at 70 °C increased the silica concentration above the critical entanglement concentration, facilitating fiber production.

Fig. 6b shows the XRD patterns of the electrospun sol–gel-derived samples. Both samples have the typical amorphous halo. The 100S was completely amorphous, while the presence of a few low intensity peaks in the 70S30C spectra suggests the presence of some crystalline phase. The crystalline peaks may be due to the $Ca(NO_3)_2$, as observed by Lin et al. [59] in sol–gel-derived glasses.

Fig. 6c shows the FTIR spectra of the 100S and 70S30C fiber samples. Bands corresponding to Si–O–Si and Si–OH were observed in both spectra. In the 70S30C spectrum, two small bands between wavenumbers 1300–1500 cm^{-1} and a small band at ~1638 cm^{-1} were also observed and assigned to ethanol and water, respectively. This indicates that there were some residual solvents trapped in the 70S30C fiber samples, confirmed by DTA/TGA curves (Fig. 6d), which show a weight loss of 12.6% around 100 °C. The FTIR does not show any evidence of unhydrolyzed TEOS, which means that the sol–gel hydrolysis and condensation reactions have successfully taken place and that the organic residues from the sol–gel precursors have also been successfully removed.

3.3. Characterization of 70S30C cotton-wool-like structure

The pore architecture of the 70S30C cotton-wool-like fibrous materials was studied with μCT and MIP. Fig. 7a shows an image of the 3-D fibrous structure of the 70S30C electrospun material after fixing it in epoxy resin. The fibers are arranged randomly in the structure, with diameters <5 μm and a very large aspect ratio. Additionally, the μCT image has close resemblance to the disordered arrangement of collagen fibers in the ECM of woven bone [60] and other tissue [4].

Low- and high-pressure MIP showed pores in the range 50 nm–300 μm (Fig. 7b). In the case of 70S30C cotton-wool-like structure, the fine entanglement of fibers produced a structure that was not penetrated by mercury at very low pressure, and, with increasing pressure, the sample began to compress under the weight of mercury. Once the entangled fibers were compressed to a sufficient packing density, where it had the strength to withstand the pressure exerted on it by the surrounding mercury, mercury began to fill in the voids between the fibers. Finally, once all the inter-fiber space had been filled, it then penetrated the smaller pores within the fibers. Fig. 7b clearly shows these three regions: (1) space between entangled fibers (>20 μm); (2) inter-fiber distance (1–20 μm); and (3) pores in the individual fibers (300–400 nm). The cumulative mercury intrusion volume is plotted as the pore fraction in per cent. This shows the percentage of void space in the sample that are the pores on the fibers (~10%), inter-fiber distance (~40%) and space between entangled fibers (~50%). It should be noted that this does not represent the porosity of the material, as porosity can be decreased by simply pressing the fibers together, or increased by pulling them apart. But for a sample that was taken off the electrospinning machine and dried at 60 °C, the pore fraction has a pattern similar to that shown in Fig. 7b.

3.4. Moldability and mechanical properties

The 70S30C cotton-wool-like material has great potential as a bone graft substitute material, particularly in dental bone regeneration. Titanium-based implants are often inserted into the jawbone as anchorage points for ceramic crowns. Often, however, there is not enough good quality bone to fix the implant into. An example is periodontal disease, where there is loss of bone in the jaw, beneath the teeth. The majority of dental implantation procedures require bone grafting before implant placement, to stabilize implants and produce bone growth. Current synthetic bioactive materials used as dental bone graft substitutes are bioactive ceramic or glass granules [61–63], which have slow and limited regeneration. Hence, healing times are very long, and the waiting time between bone grafting and implant placement can be longer

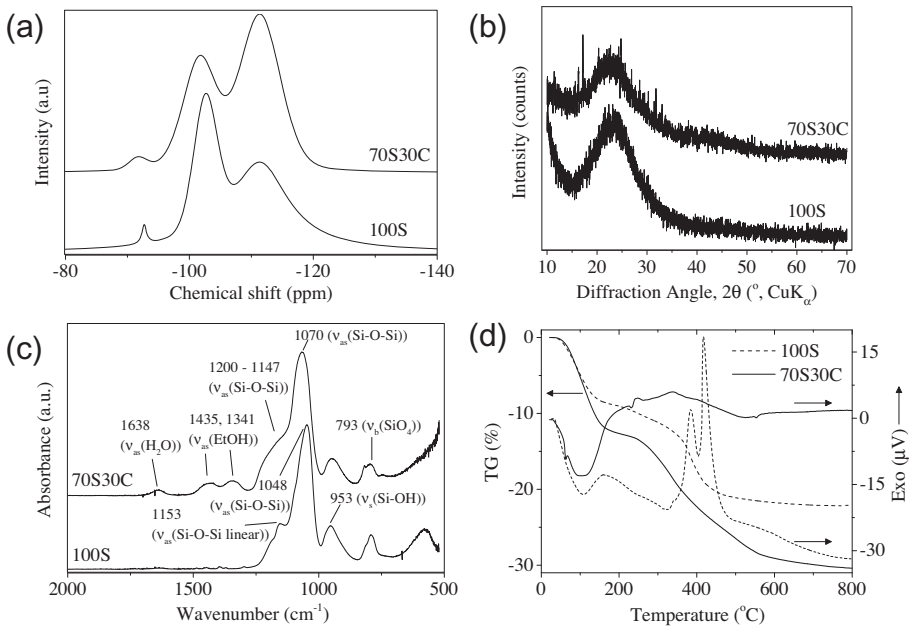

Fig. 6. (a) ^{29}Si MAS-NMR, (b) XRD and (c) FTIR spectra and (d) DTA-TGA curves of the electrospun 100S and 70S30C fibers.

Table 3
Summary of the ^{29}Si MAS-NMR spectra deconvoluted Q^n species of the 100S and 70S30C electrospun fibers.

Sample	Q^2		Q^3		Q^4		Q^3/Q^4	D_c (%)[c]
	δ[a] (ppm)	I[b] (%)	δ[a] (ppm)	I[b] (%)	δ[a] (ppm)	I[b] (%)		
100S	−92.7	1.3	−102.6	32.1	−111.4	66.6	0.48	91.3
70S30C	−91.7	1.8	−101.7	37.5	−111.4	60.7	0.62	89.7

[a] Chemical shift.
[b] Deconvoluted proportions.
[c] Degree of condensation.

than 6 months [64]. Here, 70S30C cotton-wool-like material with ECM mimicking architecture could give rise to huge improvements over the current alternatives. Once bone regeneration around the cotton wool implant has occurred, a screw-threaded implant can be inserted into the new bone (Fig. 8). A further benefit of the fiber structure is that, if unresorbed fibers remain within newly grown bone, the screw thread will still enter the new bone, whereas if hard particles remained in the bone, insertion of an implant is difficult.

The 70S30C-cotton-wool-like material has high degree of flexibility, owing to the large aspect ratio and the entanglement between the very long fibers. The handling properties of the cotton-wool-like structure were investigated by performing confined compression testing. The compressive properties of the entangled fibers are very much dependent on the extent of fiber packing, i.e. the density. To investigate the effect of density on the compressive properties of the 70S30C, confined compression tests were done on three different packing densities. Fig. 9a shows the stress–strain curves of 70S30C cotton-wool-like material packed to an initial density of 76.4, 91.2 and 114.1 kg m^{-3} and compressed to a maximum stress of 160 kPa. With increasing initial packing density, the resistance to compression was observed to increase, while the deformation before maximum stress was observed to decrease. In the literature, compression of many types of wool and simulation and modeling has shown that the loading and unloading curves exhibit significant hysteresis [65–68]. In the case of 70S30C, very little recovery was observed on unloading; this was

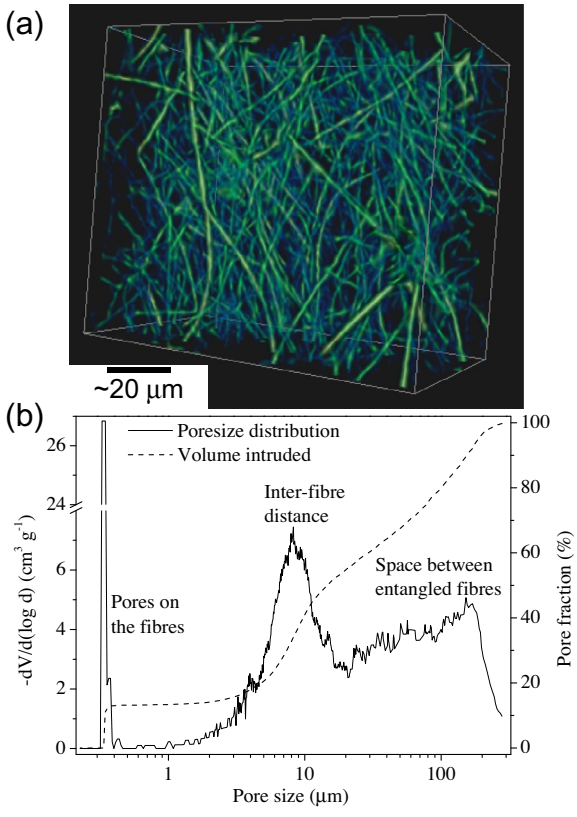

Fig. 7. (a) μCT image of a small volume of 70S30C cotton-wool-like material. (b) Pore size distribution and pore fraction obtained from MIP.

due to the breaking up of brittle fibers on compression (Supporting information 2). Van Wyk [69] proposed a theoretical model to describe the mechanics of random entangled fibrous materials under compressive pressure. This model relates the stress on the entangled mass of fibers to its density and can be written in the following form:

$$\sigma = kE_f(\rho^n - \rho_{th}^n) \quad (2)$$

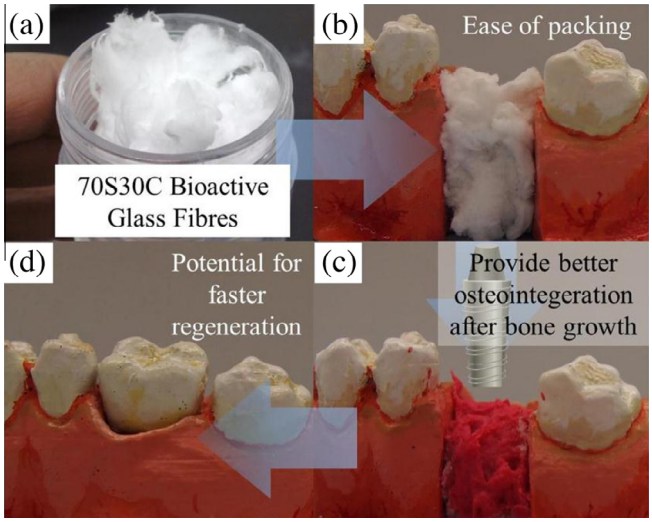

Fig. 8. Demonstration of ease of packing of (a) 70S30C cotton-wool-like material in a (b) tooth extraction socket, (c) insertion of implant following bone regeneration and (d) crown placement. The cotton-wool-like structure has significant advantages over a granular material as a dental bone graft substitute.

where σ is the stress, k is a variable constant, which depends on the orientation of the fibers and the degree of crimp, E_f is the elastic modulus of the fibers, and ρ and ρ_{th} are the current and threshold density. Van Wyk assumed that the resistance to deformation was from the bending of the fibers between contacts on other fibers. For 3-D random entangled fibrous materials, he showed that the exponent $n = 3$. Fig. 9b shows the log–log plot of stress against density for the 70S30C samples with an initial density of 76.4, 91.2 and 114.1 kg m^{-3}. The n exponent is the gradient of the straight line on the log–log plot and was calculated to be in the range 2.5–2.6 for the three samples. The n exponent calculated for 70S30C was very close to that theoretically derived by van Wyk for random entangled fibers, suggesting that the 70S30C cotton-wool-like structure behaves as a random entangled fibrous structure. Fig. 9b also shows that the n exponent for all three samples was almost identical, irrespective of the initial packing. This means that, when 70S30C cotton-wool-like material is packed into a defect, its compressive strength could easily be estimated through the packing density. Further, the lack of recovery or "bounce back" on unloading of the cotton-wool-like material is desirable for bone regeneration, since bone grafts that are mobile within the defect will slow regeneration.

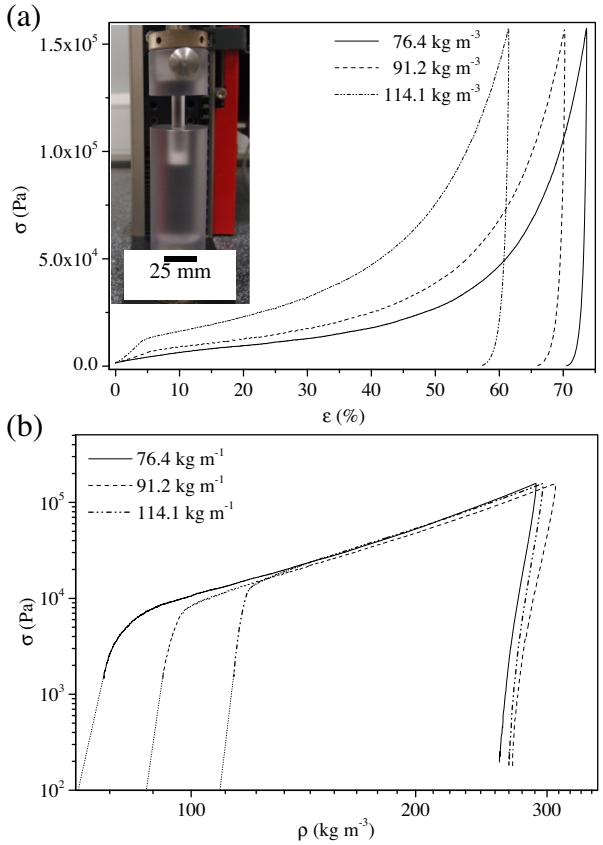

Fig. 9. Confined compression testing of 70S30C cotton-wool-like material produced (a) stress–strain behavior that is typical of 3-D wools. (b) Stress as a function of density for the 70S30C material where a power law with an exponent of 2.45–2.62 was observed. Inset in (a) shows the confined compression setup used for this experiment.

3.5. Apatite formation in SBF

HCA formation on the material in SBF is performed as the first screening test before evaluating in vivo bioactivity using animals. The time taken to deposit apatite, the thickness, coverage and the form of apatite on the material in SBF are often assessed.

Fig. 10 shows the soluble species of silica and phosphate and Ca^{2+} ion concentrations in SBF as a function of immersion time at 36.5 °C. Both samples had a slow and controlled release of soluble silica that reached a saturation concentration of ~90 μg ml^{-1} after 72 h of soaking. The silica dissolution of the 70S30C fibers was slower and more controlled than that of mesoporous bioactive glass powder of the same composition fabricated by Saravanapavan et al. [70]. The sol–gel-derived powder sintered at 700 °C with a specific surface area of 75 m^2 g^{-1} when immersed in SBF reached a soluble silica species saturation concentration of ~65 μg ml^{-1} after just 1.5 h. The saturated soluble silica concentration of the SBF after soaking 70S30C fibers was also higher than that of the powder, suggesting higher but controlled solubility of the fibers compared with the powder.

The uptake of phosphate species and Ca^{2+} ions from SBF was found to be dependent on whether the samples initially contained calcium. The soluble phosphate species concentration in SBF after soaking 100S samples showed a constant level, which means no uptake of phosphate species. Since no decrease in the concentration of phosphate species or Ca^{2+} ions was observed, apatite was not formed on the 100S fibers within the 168 h of soaking. In contrast, for the calcium-containing 70S30C samples, the phosphate species concentration in SBF steadily decreased with time. The Ca^{2+} ion concentration in SBF increased immediately after immersion of the 70S30C sample, owing to the dissolution of Ca^{2+} ion from the fibers. The Ca^{2+} ion concentration in SBF then decreased at almost a constant rate after 8 h of soaking, indicating that a calcium compound was being deposited on the fibers. These results indicate calcium phosphate deposition taking place from the moment of soaking in SBF. Saravanapavan et al. [70] found, after soaking 70S30C powder in SBF, that the Ca^{2+} ion concentration increased almost fourfold within the first 30 min and remained constant thereafter, indicating that calcium phosphate layer deposition was over within the first 30 min of soaking in SBF. In the current work, for the whole duration of the tests, the pH of SBF remained within 7.35–7.55.

Fig. 11a shows FTIR spectra of the 100S and 70S30C samples after soaking in SBF. The spectrum of 100S after 168 h of immersion was identical to that of the as-prepared material (Fig. 6c), while the double bands at ~560 and ~600 cm^{-1} associated with the P—O bond from a calcium phosphate phase were distinctly visible in the 70S30C sample after 12 h of soaking. The split double

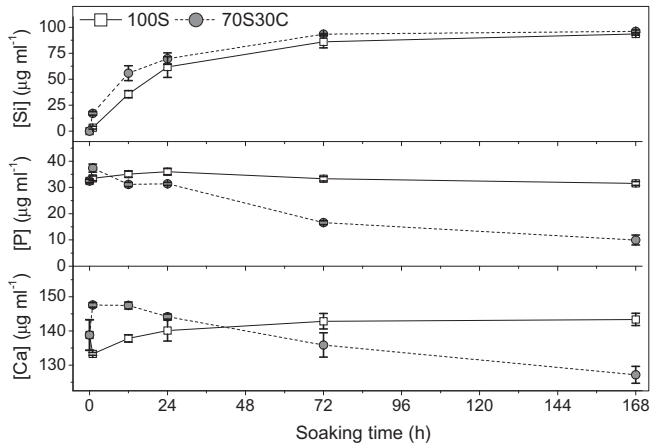

Fig. 10. Soluble silica and phosphate species and calcium concentrations in SBF after soaking the 100S and 70S30C samples as a function of time, measured using ICP-AES.

bands indicate an orthophosphate and, further, the intensity of these bands increased with longer soaking time. The 70S30C spectra in Fig. 11a also showed some very small bands at ~873, ~1417 and ~1456 cm^{-1}; these were deduced to be carbonates substituted at the phosphate site in apatite [71,72]. Fig. 11b shows the XRD patterns of the 100S and 70S30C samples after soaking in SBF. Sodium chloride diffraction peaks at 2θ 27.3°, 31.6°, 45.4°, 56.5° and 66.2° (pdf file no. 00-005-0628) were found on all the samples, which was an artifact of the SBF test. A larger amorphous halo was observed on 100S–168 h compared with 70S30C at all the time points. There was no apatite formation on 100S. The 70S30C had a broad peak at the site of the primary peak of hydroxyapatite (2θ = 31.774° (d_{211})) after 12 h of soaking. The intensity of this broad peak increased after 24 h, and a new peak at 25.8° (d_{002}) was also observed. After 72 and at 168 h of soaking, the intensity of all the peaks increased, and new peaks at 34.2° (d_{202}) and 39.5° (d_{130}) corresponding to HA were also observed.

Another important peak, which is usually the second most intense peak of HA at 32.9° associated with the d_{300} spacing and is usually more intense than the peak at 2θ 25.8° (d_{002}), was only faintly visible in the XRD pattern in Fig. 11b. This is due to the substitution of PO_4 tetrahedron by carbonate, which shortens the *a*-axis of the HA unit cell, hence its intensity is decreased, as observed by Chickerur et al. [72]. The XRD results therefore confirm the FTIR observations, where a carbonate substituted hydroxyapatite forms on 70S30C samples after 12 h of soaking in SBF, which matures into a crystalline HCA by 72 h.

Quintero et al. [40] produced bioactive glass nanofibers with the melt-derived Bioglass composition (46.1 mol.% SiO_2, 26.9 mol.% CaO, 24.4 mol.% Na_2O and 2.5 mol.% P_2O_5) by laser-spinning, which were shown to be highly bioactive, with calcium phosphate deposition being observed after 12 h of immersion in SBF. However, they found that the fibers had completely dissolved after only 48 h of soaking in SBF, leaving a hollow tube of apatite [40]. In the 70S30C sol–gel fibers, the amorphous halo seen in the XRD pattern in Fig. 11b decreased as soaking time increased, but a significant amorphous halo was still visible after 168 h of soaking.

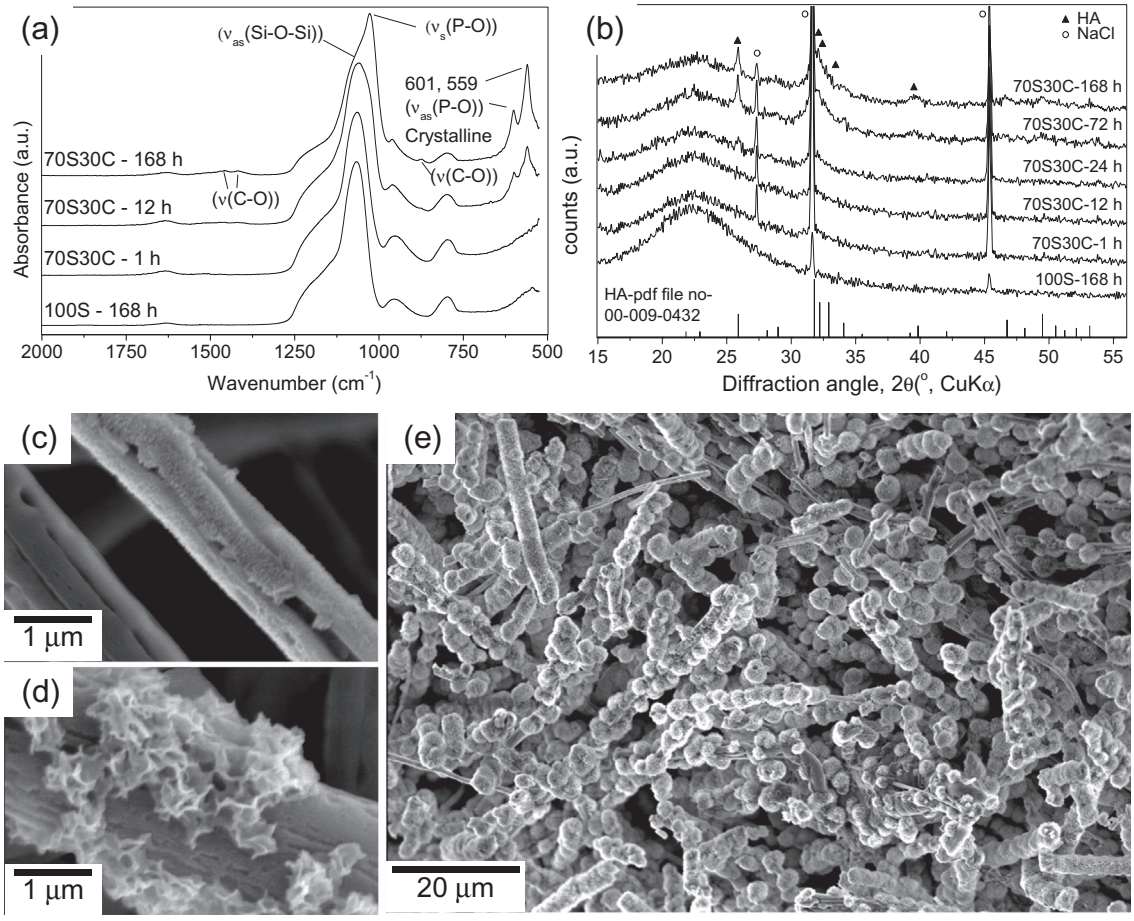

Fig. 11. Results of the 100S and 70S30C samples after soaking in SBF. (a) FTIR spectra of samples after soaking, (b) XRD pattern of synthetic HA (pdf file no. 00-009-0432) and sol–gel fibrous samples 100S and 70S30C after soaking in SBF and SEM images of 70S30C fibers after soaking in SBF for (c) 1 h, (d) 12 and (e) 72 h.

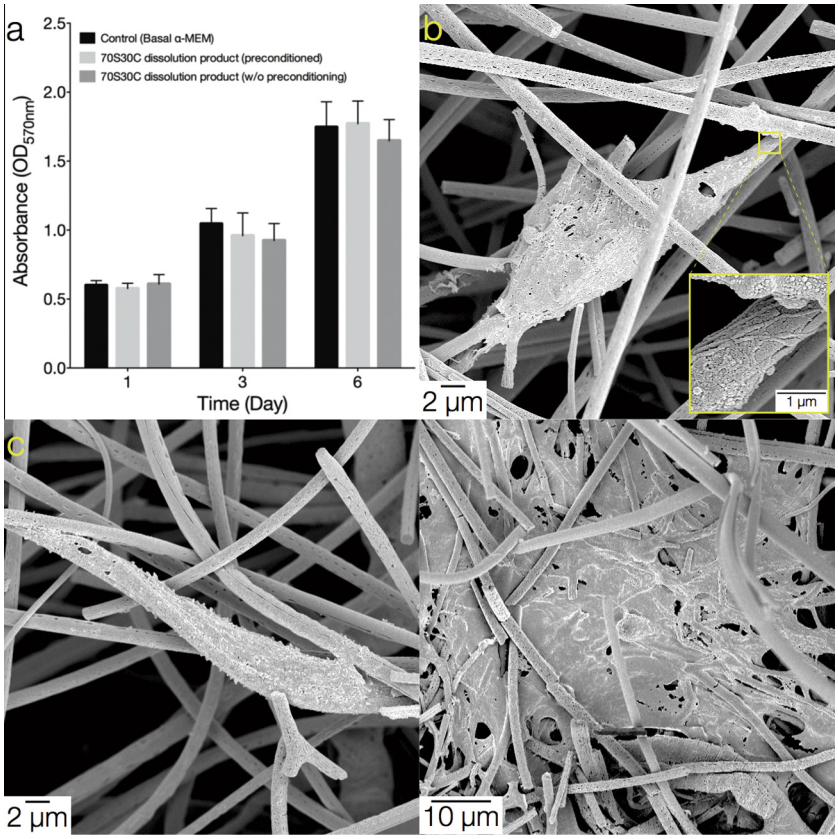

Fig. 12. (a) Cellular metabolic activity over a period of 7 days for MC3T3-E1 preosteoblast cells cultured in the presence of dissolution products of 70S30C cotton-wool-like material. Data are expressed as the mean ± SD from three independent experiments. (b–d) SEM micrographs of MC3T3-E1 preosteoblasts cultured on 70S30C cotton-wool-like fibrous scaffolds. The cellular compatibility of the scaffolds was evident, as demonstrated by (a) cell attachment and spreading and (b) deposition of ECM following 3-day culture period.

Therefore, the sol–gel-derived silica fibers remained even after soaking for 168 h. The fast resorption of the laser-spun Bioglass was due to the low coordination of the silica species (D_c < 50%). The sol–gel-derived glasses have much higher silica coordination (D_c > 87%) [51] and hence a slower degradation of the silica species, even though they have a high surface area to volume ratio and accelerated HCA formability.

Fig. 11c–e shows low and high magnification SEM images of the 70S30C samples after soaking in SBF. The low magnification image in Fig. 11e shows that the majority of the fibers were coated with HCA after 72 h of soaking; the deposited material has the typical globular cauliflower-like morphology for the HCA as often found in bioactive glasses and appears attached to the surface of the fibers [73]. Fig. 11c shows part of two fibers that were soaked in SBF for 1 h: one of the fibers is completely covered by a layer of newly deposited material. Although, XRD showed that NaCl was present in the samples after 1 h of soaking, NaCl crystals have a distinct cubic structure, and therefore the newly deposited material is not NaCl. After 12 h of soaking (Fig. 11d), the fibers also appear coated with the fine nanoparticles, but a few larger particles of a different morphology are also observed. The newly formed particles were plate-like and seem to be the precursor to the globular cauliflower-like HCA particle. The cauliflower-like particles after 24 h of soaking were observed to be ~2 μm, which grew to ~3 μm and finally ~5 μm after soaking for 72 and 168 h, respectively. The SEM images also support the FTIR and XRD pattern results, where rapid deposition of a new material on the fibers took place, which by 72 h matured into crystalline HCA.

Therefore, to summarize, on soaking the 70S30C samples in SBF, first an amorphous calcium phosphate phase was rapidly deposited on the fibers. The amorphous calcium phosphate phase then transformed into crystalline HCA.

3.6. Cell attachment and viability

Cell viability was assessed by measuring the metabolic activity of MC3T3-E1 cells. The MTT assay confirmed that the 70S30C cotton-wool-like fibrous material was not toxic to the cells even without preconditioning. Furthermore, cells were capable of growth steadily over a period of 7 days in the presence of dissolution products of 70S30C cotton-wool-like fibrous scaffolds (Fig. 12a). The ICP results demonstrated that the dissolution products of 70S30C cotton-wool-like fibrous scaffolds contained Ca^{2+} at a concentration comparable with α-MEM culture media (Supporting information 3). Standard α-MEM did not contain Si species and, therefore, 70S30C cotton-wool-like fibrous scaffolds produced the increase in the Si species level of the media. These findings suggest that Si dissolution products from the fibers have a more profound stimulatory effect on the formation of ECM. Similar observations were made in previously published studies using 70S30C foam [74]. Cell attachment and distribution on the electrospun scaffolds were examined by SEM. At day 3, MC3T3-E1 preosteoblasts attached to and spread across the 70S30C fiber network with evident presence of discrete filopodia (Fig. 12b, c), indication of cellular compatibility of the scaffold material to support cell attachment and proliferation. In regions where cell clusters were present, ECM was seen covering the fiber network (Fig. 12d). Furthermore, a layer of crystalline particles was seen on the cell surface. These observations suggest that the 70S30C cotton-wool-like fibrous scaffolds have the potential to induce ECM deposition without

the presence of ascorbic acid and dexamethasone, which are common supplements when studying in vitro osteogenic differentiation. Further studies, however, are required to confirm osteogenic differentiation and bone matrix formation of cells in 70S30C cotton-wool-like fibrous scaffolds.

4. Conclusions

The production of the first flexible electrospun 3-D cotton-wool-like structure was demonstrated through a combination of sol–gel and electrospinning. Electrospun sol–gel-derived inorganic materials with relatively homogeneous fiber diameter were prepared without the use of a polymer binding agent; this is highly advantageous, owing to the avoidance of post-processing of fibers. The mechanism of formation of the cotton-wool-like structure was also explained and was reliant on the presence of calcium ions. Micro-CT and MIP showed the presence of three orders of porosity in the 70S30C material; pores on the fibers, pores between fibers and pores in the entangled fiber space. This hierarchy of porosity could enhance cellular attachment and migration among the fibers of the scaffold. Compression testing showed that the 70S30C material behaved in similar fashion to a randomly oriented entangled material, such as wool, and that the stress is related to the density through a power law.

The calcium-containing electrospun sol–gel-derived 70S30C fibers showed rapid apatite formation in SBF, where deposition of a calcium phosphate phase was observed after an hour of soaking. The fast kinetics of HCA formation was owing to both the sol–gel and the electrospinning process. The 70S30C cotton-wool-like material demonstrated no adverse cytotoxic effect and was capable of supporting cell attachment and spread.

Acknowledgements

The authors are indebted to Mr. H. Kato for assistance with NMR and to Mr. T.B. Kim for assistance with the Avizo visualization package. The present work was supported in part by a grant from Institute of Ceramics Research and Education, NITECH and the JSPS International Training Program. The EPSRC is thanked for funding (EP/E051669/1, EP/I020861/1 and providing space at the Research Complex at Harwell via EP/I02249X/1).

Appendix A. Figures with essential color discrimination

Certain figures in this article, particularly Figs. 3–5, 7–9 and 12 are difficult to interpret in black and white. The full color images can be found in the on-line version, at http://dx.doi.org/10.1016/j.actbio.2014.05.020.

Appendix B. Supplementary data

Supplementary data associated with this article can be found, in the online version, at http://dx.doi.org/10.1016/j.actbio.2014.05.020.

References

[1] Gentili C, Cancedda R. Cartilage and bone extracellular matrix. Curr Pharm Des 2009;15:1334–48.
[2] Marastoni S, Ligresti G, Lorenzon E, Colombatti A, Mongiat M. Extracellular matrix: a matter of life and death. Connect Tissue Res 2008;49:203–6.
[3] Xiao G, Gopalakrishnan R, Jiang D, Reith E, Benson MD, Francesch RT. Bone morphogenetic proteins, extracellular matrix, and mitogen-activated protein kinase signaling pathways are required for osteoblast-specific gene expression and differentiation in MC3T3-E1 cells. J Bone Miner Res 2002;17:101–10.
[4] Brightman AO, Rajwa BP, Sturgis JE, McCallister ME, Robinson JP, Voytik-Harbin SL. Time-lapse confocal reflection microscopy of collagen fibrillogenesis and extracellular matrix assembly in vitro. Biopolymers 2000;54:222–34.
[5] Benders KE, van Weeren PR, Badylak SF, Saris DB, Dhert WJ, Malda J. Extracellular matrix scaffolds for cartilage and bone regeneration. Trends Biotechnol 2013;31:169–76.
[6] Jones JR, Lee PD, Hench LL. Hierarchical porous materials for tissue engineering. Philos Transact Math Phys Eng Sci 2006;364:263–81.
[7] Hench LL, Polak JM. Third-generation biomedical materials. Science 2002;295:1014–7.
[8] Reneker DH, Chun I. Nanometre diameter fibres of polymer, produced by electrospinning. Nanotechnology 1996;7:216–23.
[9] Li D, Xia Y. Electrospinning of nanofibers: reinventing the wheel? Adv Mater 2004;16:1151–70.
[10] Bhardwaj N, Kundu SC. Electrospinning: a fascinating fiber fabrication technique. Biotechnol Adv 2010;28:325–47.
[11] Stevens MM, George JH. Exploring and engineering the cell surface interface. Science 2005;310:1135–8.
[12] Liang D, Hsiao BS, Chu B. Functional electrospun nanofibrous scaffolds for biomedical applications. Adv Drug Deliv Rev 2007;59:1392–412.
[13] Park S, Park K, Yoon H, Son JG, Min T, Kim GH. Apparatus for preparing electrospun nanofibers: designing an electrospinning process for nanofiber fabrication. Polym Int 2007;56:1361–6.
[14] Xie J, Li X, Xia Y. Putting electrospun nanofibers to work for biomedical research. Macromol Rapid Commun 2008;29:1775–92.
[15] Jang JH, Castano O, Kim HW. Electrospun materials as potential platforms for bone tissue engineering. Adv Drug Deliv Rev 2009;61:1065–83.
[16] Zhang YZ, Su B, Venugopal J, Ramakrishna S, Lim CT. Biomimetic and bioactive nanofibrous scaffolds from electrospun composite nanofibers. Int J Nanomed 2007;2:623–38.
[17] Matthews JA, Wnek GE, Simpson DG, Bowlin GL. Electrospinning of collagen nanofibers. Biomacromolecules 2002;3:232–8.
[18] Tan SH, Inai R, Kotaki M, Ramakrishna S. Systematic parameter study for ultra-fine fiber fabrication via electrospinning process. Polymer 2005;46:6128–34.
[19] Lee SJ, Yoo JJ, Lim GJ, Atala A, Stitzel J. In vitro evaluation of electrospun nanofiber scaffolds for vascular graft application. J Biomed Mater Res A 2007;83:999–1008.
[20] Zhang Y, Ouyang H, Lim CT, Ramakrishna S, Huang ZM. Electrospinning of gelatin fibers and gelatin/PCL composite fibrous scaffolds. J Biomed Mater Res B Appl Biomater 2005;72:156–65.
[21] Poologasundarampillai G, Yu B, Jones JR, Kasuga T. Electrospun silica/PLLA hybrid materials for skeletal regeneration. Soft Matter 2011;7:10241–51.
[22] Saravanapavan P, Hench LL. Low-temperature synthesis, structure, and bioactivity of gel-derived glasses in the binary $CaO–SiO_2$ system. J Biomed Mater Res 2001;54:608–18.
[23] Vallet-Regi M, Arcos D. Nanostructured hybrid materials for bone tissue regeneration. Curr Nanosci 2006;2:179–89.
[24] Jones JR, Ehrenfried LM, Hench LL. Optimising bioactive glass scaffolds for bone tissue engineering. Biomaterials 2006;27:964–73.
[25] Dai X, Shivkumar S. Electrospinning of hydroxyapatite fibrous mats. Mater Lett 2007;61:2735–8.
[26] Kim HW, Kim HE, Knowles JC. Production and potential of bioactive glass nanofibers as a next-generation biomaterial. Adv Funct Mater 2006;16:1529–35.
[27] Sakai S, Yamada Y, Yamaguchi T, Kawakami K. Prospective use of electrospun ultra-fine silicate fibers for bone tissue engineering. Biotechnol J 2006;1:958–62.
[28] Peltola T, Jokinen M, Veittola S, Rahiala H, Yli-Urpo A. Influence of sol and stage spinnability on in vitro bioactivity and dissolution of sol–gel-derived SiO_2 fibers. Biomaterials 2001;22:589–98.
[29] Xia W, Zhang D, Chang J. Fabrication and in vitro biomineralization of bioactive glass (BG) nanofibres. Nanotechnology 2007;18:135601.
[30] Lu H, Zhang T, Wang XP, Fang QF. Electrospun submicron bioactive glass fibers for bone tissue scaffold. J Mater Sci Mater Med 2009;20:793–8.
[31] Hong Y, Chen X, Jing X, Fan H, Guo B, Gu Z, et al. Preparation, bioactivity, and drug release of hierarchical nanoporous bioactive glass ultrathin fibers. Adv Mater 2010;2010:6.
[32] Lu H, Zhang T, Wang XP, Fang QF. Electrospun submicron bioactive glass fibers for bone tissue scaffold. J Mater Sci Mater Med 2009;20:793–8.
[33] Ma Z, Dong G, Lv C, Qi J. Core–shell glass fibers with high bioactivity and good flexibility. Mater Lett 2012;88:136–9.
[34] Yamaguchi T, Sakai S, Kawakami K. Application of silicate electrospun nanofibers for cell culture. J Sol-Gel Sci Technol 2008;48:350–5.
[35] Hulbert S, Morrison S, Klawitte J. Tissue reaction to 3 ceramics of porous and non-porous structures. J Biomed Mater Res 1972;6:347.
[36] Fujikura K, Obata A, Kasuga T. Cellular migration to electrospun poly(lactic acid) ibermats. J Biomater Sci Polym Ed 2011;23:1939–50.
[37] Kim G, Kim W. Highly porous 3D nanofiber scaffold using an electrospinning technique. J Biomed Mater Res B Appl Biomater 2007;81:104–10.
[38] Ki CS, Park SY, Kim HJ, Jung HM, Woo KM, Lee JW, et al. Development of 3-D nanofibrous fibroin scaffold with high porosity by electrospinning: implications for bone regeneration. Biotechnol Lett 2008;30:405–10.
[39] Ji Y, Ghosh K, Shu XZ, Li B, Sokolov JC, Prestwich GD, et al. Electrospun three-dimensional hyaluronic acid nanofibrous scaffolds. Biomaterials 2006;27:3782–92.
[40] Quintero F, Pou J, Comesaña R, Lusquiños F, Riveiro A, Mann AB, et al. Laser spinning of bioactive glass nanofibers. Adv Funct Mater 2009;19:3084–90.

[41] Jung SB, Day DE. Scaffolds with trace element for tissue regeneration in mammals. WO/2011/0087772011.
[42] Schneider OD, Loher S, Brunner TJ, Uebersax L, Simonet M, Grass RN, et al. Cotton wool-like nanocomposite biomaterials prepared by electrospinning: in vitro bioactivity and osteogenic differentiation of human mesenchymal stem cells. J Biomed Mater Res 2008;84B:350–62.
[43] Obata A, Ozasa H, Kasuga T, Jones JR. Cotton wool-like poly(lactic acid)/vaterite composite scaffolds releasing soluble silica for bone tissue engineering. J Mater Sci Mater Med 2013;24:1649–58.
[44] Sacks MD, Sheu RS. Rheological properties of silica sol–gel materials. J Non-Cryst Solids 1987;92:383–96.
[45] Sakka S. Fibers from the sol–gel process. In: Klein LC, editor. Sol–Gel technology for thin films, fibers, preforms, electronics and specialty shapes. Saddle River, NJ: Noyes Publications; 1988. p. 407.
[46] Sakka S, Kamiya K. The sol–gel transition in the hydrolysis of metal alkoxides in relation to the formation of glass fibers and films. J Non-Cryst Solids 1982;48:31–46.
[47] Massiot D, Fayon F, Capron M, Alonso B, Durand JO, Bujoli B, et al. Modelling one and two-dimensional solid-state NMR spectra. Magn Reson Chem 2002; 40:70–6.
[48] Kokubo T, Kushitani H, Sakka S, Kitsugi T, Yamamuro T. Solutions able to reproduce in vivo surface-structure changes in bioactive glass-ceramic A-W3. J Biomed Mater Res 1990;24:721–34.
[49] Kokubo T, Takadama H. How useful is SBF in predicting in vivo bone bioactivity? Biomaterials 2006;27:2907–15.
[50] Mosmann T. Rapid colorimetric assay for cellular growth and survival: application to proliferation and cytotoxicity assays. J Immunol Methods 1983;65:55–63.
[51] Lin S, Ionescu C, Pike KJ, Smith ME, Jones JR. Nanostructure evolution and calcium distribution in sol–gel derived bioactive glass. J Mater Chem 2009;19:1276–82.
[52] Reneker DH, Yarin AL, Fong H, Koombhongse S. Bending instability of electrically charged liquid jets of polymer solutions in electrospinning. J Appl Phys 2000;87:4531–47.
[53] Reneker DH, Yarin AL. Electrospinning jets and polymer nanofibers. Polymer 2008;49:2387–425.
[54] Yarin AL, Kataphinan W, Reneker DH. Branching in electrospinning of nanofibers. J Appl Phys 2005;98:064501.
[55] Zong X, Kim K, Fang D, Ran S, Hsiao BS, Chu B. Structure and process relationship of electrospun bioabsorbable nanofiber membranes. Polymer 2002;43:4403–12.
[56] Srinivasan G. Structure and morphology of electrospun polymer fibers, The University of Akron, 1994.
[57] Shenoy SL, Bates WD, Frisch HL, Wnek GE. Role of chain entanglements on fiber formation during electrospinning of polymer solutions: good solvent, non-specific polymer–polymer interaction limit. Polymer 2005;46:3372–84.
[58] McKee MG, Layman JM, Cashion MP, Long TE. Phospholipid nonwoven electrospun membranes. Science 2006;311:353–5.
[59] Lin S, Baker S, Jones JR. Characterisation of the inhomogeneity of sol–gel-derived SiO_2–CaO bioactive glass and a strategy for its improvement. J Sol-Gel Sci Technol 2010;53:255–62.
[60] Martin BR, Burr BD. Structure, function, and adaptation of compact bone. New York: Raven Press; 1989.
[61] Dumitrescu LA. Bone grafts and bone graft substitutes in periodontal therapy. Chemicals in surgical periodontal therapy. Berlin: Springer; 2011 [pp. 73–127].
[62] Aiken S, Bendkowski A. In search of the "optimal" material for dental bone grafting. Eur J Dent Implantol 2011;4:42–8.
[63] Taba MJ, Jin Q, Sugai JVG, Giannobile WV. Current concepts in periodontal bioengineering. Orthod Cranofac Res 2005;8:292–302.
[64] Bartee BK. Extraction site reconstruction for alveolar ridge preservation. Part 1. Rationale and materials selection. J Oral Implantol 2001;27:187–93.
[65] Picu CR. Mechanics of random fiber networks – a review. Soft Matter 2011;7:6768–85.
[66] Masse JP, Salvo L, Rodney D, Bréchet Y, Bouaziz O. Influence of relative density on the architecture and mechanical behaviour of a steel metallic wool. Scripta Mater 2006;54:1379–83.
[67] Poquillon D, Viguier B, Andrieu E. Experimental data about mechanical behaviour during compression tests for various matted fibres. J Mater Sci 2005;4:5963–70.
[68] Subramanian G, Picu CR. Mechanics of three-dimensional, nonbonded random fiber networks. Phys Rev E Stat Nonlin Soft Matter Phys 2011;83:056120.
[69] Van Wyck CM. 20-Note on the compressibility of wool. J Textile Inst Transact 1946;37:T285–92.
[70] Saravanapavan P, Jones JR, Pryce RS, Hench LL. Bioactivity of gel–glass powders in the CaO–SiO_2 system: a comparison with ternary (CaO–P_2O_5–SiO_2) and quaternary glasses (SiO_2–CaO–P_2O_5–Na_2O). J Biomed Mater Res A 2003;66: 110–9.
[71] Jackson KDO. A guide to identifying common inorganic fillers and activators using vibrational spectroscopy. Internet J Vibrational Spectrosc. UK 1998;2. http://www.ijvs.com/volume2/edition3/section3.html.
[72] Chickerur NS, Tung MS, Brown WE. A mechanism for incorporation of carbonate into apatite. Calcif Tissue Int 1980;32:55–62.
[73] Clupper DC, Gough JE, Hall MM, Clare AG, LaCourse WC, Hench LL. In vitro bioactivity of S520 glass fibers and initial assessment of osteoblast attachment. J Biomed Mater Res 2003;67:285–94.
[74] Jones JR, Tsigkou O, Coates EE, Stevens MM, Polak JM, Hench LL. Extracellular matrix formation and mineralization on a phosphate-free porous bioactive glass scaffold using primary human osteoblast (HOB) cells. Biomaterials 2007;28:1653–63.